Chinese Journal of Aeronautics, (2025), 38(5): 103390

Chinese Society of Aeronautics and Astronautics
& Beihang University

Chinese Journal of Aeronautics

cja@buaa.edu.cn
www.sciencedirect.com

COVER ARTICLE

Coupled aeroelastic analysis of a panel in supersonic flow with add-on acoustic black hole

Zhuogeng ZHANG [a], Hongli JI [a,*], Jinhao QIU [a], Kaihua YUAN [b], Li CHENG [c]

[a] College of Aerospace Engineering, Nanjing University of Aeronautics and Astronautics, Nanjing 210016, China
[b] Beijing Institute of Mechanical and Electrical Engineering, Beijing 100074, China
[c] Department of Mechanical Engineering, Hong Kong Polytechnic University, Hong Kong 999077, China

Received 6 May 2024; revised 13 June 2024; accepted 25 August 2024
Available online 2 January 2025

KEYWORDS

Panel flutter;
Acoustic black hole;
Flutter suppression;
Coupled analysis;
Aeroelastic

Abstract This study introduces a novel approach for coupled aeroelastic analysis of panel subjected to supersonic airflow, utilizing Add-On Acoustic Black Hole (AABH) to mitigate panel flutter. Employing Galerkin's method to discretize aeroelastic equation of panel and leveraging finite element method to derive a reduced discrete model of AABH, this study effectively couples two substructures via interface displacement. Investigation into the interactive force highlights the modal effective mass, frequency discrepancy between oscillation and AABH mode, and modal damping ratio as critical factors influencing individual AABH mode in flutter suppression. The selection of effective AABH modes, closely linked to these factors, directly influences the accuracy of simulations. The results reveal that AABH notably enhances the panel's critical flutter boundary by 14.6%, a significant improvement over the 3.6% increase afforded by equivalent mass. Furthermore, AABH outperforms both the tuned mass damper and nonlinear energy sink in flutter suppression efficacy. By adjusting the AABH's geometrical parameters to increase the accumulative modal effective mass within the pertinent frequency range, or choosing a suitable installation position for AABH, its performance in flutter suppression is further optimized. These findings not only underscore the AABH's potential in enhancing aeroelastic stability but also provide a foundation for its optimal design.

1. Introduction

Panel flutter is a typically dynamic aeroelastic instability phenomenon of the external skin panel with one side exposed to supersonic airflow.[1] This phenomenon can lead to fatigue damage in panel structures and result in serious consequences for the panel flutter is characterized by low-amplitude and long-lasting vibration.[2] Therefore, how to suppress panel flutter and reduce the vibration amplitudes is an urgent problem

* Corresponding author.
E-mail address: jihongli@nuaa.edu.cn (H. JI).

Peer review under responsibility of Editorial Committee of CJA

ELSEVIER Production and hosting by Elsevier

https://doi.org/10.1016/j.cja.2024.103390

to be solved. In the past, a lot of research has been devoted to either suppress flutter or reduce the vibration amplitudes. It has been proved that active control with smart materials can be used to suppress the aeroelastic response of panels.[3–6] However, active control is limited by its requirements in terms of energy or space for actuators and sensors. Furthermore, delays in signal transmission can reduce the performance of the control system, or even generate unexpected instabilities. So, many effective passive control methods have been proposed to suppress the panel flutter.[7–9] Specifically, the linear Tuned Mass Damper (TMD), which can have a significant control effect of panel flutter in a specific narrow frequency band, has been widely studied.[10] To broaden the effective frequency band, a Nonlinear Energy Sink (NES) comprises a small mass, a linear damper, and a nonlinear spring, has been proposed. For example, Pacheco et al.[11] found that when the dynamic pressure is greater than the critical flutter pressure within a certain range, NES can completely suppress the limit cycle motion of the panel. And NES has shown promise for aeroelastic suppression, demonstrating its feasibility through theoretical analysis and experimental validation.[12,13] This is because the NES can efficiently capture the vibration energy of the main structure, transfer it to itself, and finally dissipate it through damping elements.[14,15] While NES presents effective and versatile performance,[16–18] it may face limitations under large-scale excitation,[19] and since the nonlinear spring, the vibration amplitude of the panel cannot be completely suppressed before reaching the critical flutter boundary. The strict installation requirements also can be challenging to meet in practical engineering scenarios.

In contract to traditional vibration absorber, Acoustic Black Hole (ABH) structures have been drawing attention due to its advantages of light weight, high damping capability and easy implementation.[20–22] ABH, as a passive damping technique for vibration reduction, leveraging their unique energy concentration in flexural wave propagation, achieve superior energy dissipation by integrating damping materials in high-energy zones. To circumvent the static limitations of ABH due to diminishing thickness, the concept of an Add-on ABH (AABH) merges dynamic vibration and waveguide absorber benefits. Various AABH designs, including 1-D beams, circular, eccentric, and planar swirl-shaped absorbers, have been rigorously analyzed for acoustic-vibration control,[23–26] offering innovative solutions for panel flutter suppression.

Traditional vibration control is determined by the inherent characteristics of the structure, specifically the mode shapes and frequencies associated with each mode. AABH primarily achieves vibration reduction by utilizing its high damping characteristics and the dynamic interactions with the main structure at specific frequencies caused by its diverse modes. In contrast, the aeroelastic response of the panel is distinct. It deviates from the frequencies and vibration modes corresponding to its modes due to the influence of aerodynamic forces. Additionally, the vibration undergoes continuous variations with changes in the inflow. These factors pose increased challenges for flutter suppression using conventional passive control structures.

Compared with traditional passive control structures, the AABH's rich modal characteristics and high mode density can be interpreted as an ensemble of multiple linear TMDs targeting different frequencies, increasing the likelihood of interaction with the main structure, and the damping enhancement due to ABH-specific energy trapping near these frequencies can yield superior results.[24] Refer to the suppression principle of NES, AABH has the advantageous traits of transferring energy from the main structure to itself and dissipating energy through damping elements, and the lack of nonlinear component in AABH as opposed to the nonlinear spring used in NES, which exhibits much simpler linear dynamic responses that could be beneficial when applied to suppress flutter. In the past, we were the first to propose and validate the feasibility of using AABH for flutter suppression through fluid–structure interaction calculations in commercial software, and the detailed analysis of its effects from an energy perspective is conducted.[27]

However, incorporating AABH into panel structures for the prediction of aerodynamic response and flutter pressure presents a complex challenge, requiring a sophisticated numerical strategy. The slow convergence rates of supersonic flow simulations, coupled with the detailed meshing needed for AABH, make the use of commercial finite element software highly time-consuming. Additionally, there are significant limitations when it comes to performing comparative calculations and analysis of various parameters. Although many models for aeroelastic calculations have been proposed in the past,[28,29] unfortunately, none of them can be applied to the calculation of panel with AABH. To overcome the drawbacks associated with commercial software in analyzing panel systems equipped with AABH, this study introduces an innovative fluid–structure coupling numerical method. This method seamlessly integrates the continuous displacement and interaction forces between the panel structure and the AABH, crafting a fluid–structure coupled aeroelastic model that includes an add-on acoustic black hole. The panel's aeroelastic model is discretized using Galerkin's method and solved through numerical integration, offering insights into the panel's dynamic behavior and aerodynamic force response, and enabling precise predictions of its critical flutter boundary. Furthermore, a reduced discrete model of the AABH is derived via FEM analysis and numerical modal decomposition, with both subsystems being interconnected through interface displacement and resolved using alternate numerical integration techniques.

The paper is organized as follows: Section 2 formulates the aeroelastic equations for a 3-D panel equipped with an AABH and validates the model. Section 3 delves into the AABH structure's computational convergence, its aeroelastic response, and the areas where flutter is suppressed. Section 4 discusses the mechanism behind flutter suppression, focusing on the energy transfer between the panel and AABH, and contrasts the efficacy of AABH with traditional passive controls. The paper concludes with Section 5, summarizing the findings and implications of the study.

2. Aeroelastic analysis of a 3-D panel with an AABH

2.1. Governing equations and their solution for a 3-D panel

The aeroelastic model of the four-side simply supported 3-D panel with an AABH is shown in Fig. 1. The length, width and thickness of the panel are a, b, and h respectively.(x_A, y_A) is the installed position of the AABH. By integrating von Karman's large deformation theory, aerodynamic loads p_a approx-

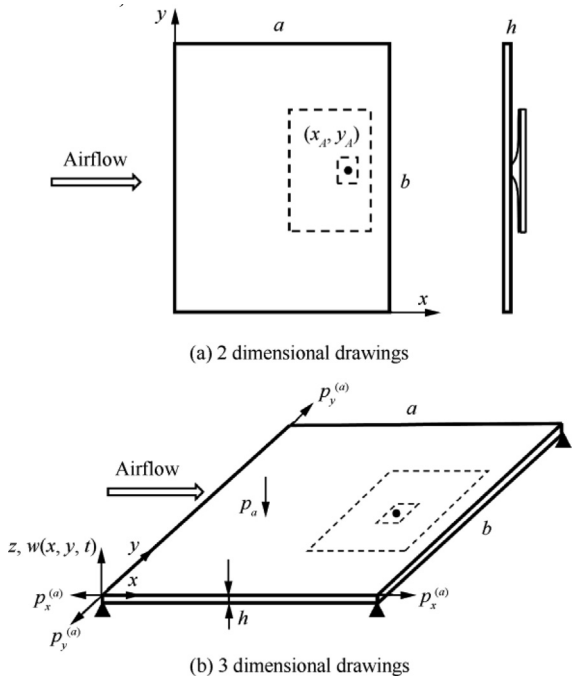

Fig. 1 Schematic of 3-D panel with an AABH structure.

imated by first-order piston theory, the in-plane external loads $p_x^{(a)}$, $p_y^{(a)}$, and the forces F_{AABH} exerted on the panel by the AABH, the aeroelastic equations for a 3-D panel with an AABH[30] is established, which can be written as follows:

$$\begin{aligned}&\frac{D}{h}\left(\frac{\partial^4 w}{\partial x^4}+2\frac{\partial^4 w}{\partial x^2\partial y^2}+\frac{\partial^4 w}{\partial y^4}\right)=\\&\frac{1}{h}\left(\frac{\partial^2\varphi}{\partial y^2}\cdot\frac{\partial^2 w}{\partial x^2}-2\frac{\partial^2\varphi}{\partial x\partial y}\cdot\frac{\partial^2 w}{\partial x\partial y}+\frac{\partial^2\varphi}{\partial x^2}\cdot\frac{\partial^2 w}{\partial y^2}\right.\\&\left.+p_x^{(a)}\frac{\partial^2 w}{\partial x^2}+p_y^{(a)}\frac{\partial^2 w}{\partial y^2}\right)-\rho\frac{\partial^2 w}{\partial t^2}+\frac{p_a}{h}\\&+\frac{F_{\mathrm{AABH}}}{h}\delta[(x-x_A)(y-y_A)]\end{aligned}\tag{1}$$

$$\begin{aligned}&\frac{1}{Eh}\left(\frac{\partial^4\varphi}{\partial x^4}+2\frac{\partial^4\varphi}{\partial x^2\partial y^2}+\frac{\partial^4\varphi}{\partial y^4}\right)=\\&\left(\frac{\partial^2 w}{\partial x\partial y}\right)^2-\frac{\partial^2 w}{\partial x^2}\cdot\frac{\partial^2 w}{\partial y^2}\end{aligned}\tag{2}$$

where, the Eq. (1) is the equilibrium equation and the Eq. (2) is the consistency equation, jointly forming the coupled system for displacement w and Airy stress potential φ function. $D=Eh^3/12(1-\upsilon^2)$ denotes the bending stiffness of the panel, E signifies Young's modulus, υ is Poisson's ratio, and ρ represents the panel's density. It should be noted that the dynamic effect of the AABH is model as a reactive force.

The aerodynamic load is calculated by the quasi-steady first-order piston theory, which can be expressed as:

$$p_a=-\frac{2p}{\beta}\left(\frac{\partial w}{\partial x}+\frac{Ma^2-2}{Ma^2-1}\cdot\frac{1}{V_\infty}\cdot\frac{\partial w}{\partial t}\right)\tag{3}$$

where $p=\rho_a V_\infty^2/2$ is the dynamic pressure. ρ_a and V_∞ are the air density and the far field airflow velocity, respectively. Ma is the Mach number. $\beta=\sqrt{Ma^2-1}$ is the Prandtl-Glauert parameter.

Eq. (1) and Eq. (2) can be transformed into non-dimensional form utilizing the non-dimensional variables outlined in Appendix A, yielding the following non-dimensional equations:

$$\begin{aligned}&\frac{\partial^4\bar{w}}{\partial\xi^4}+2s_b^2\frac{\partial^4\bar{w}}{\partial\xi^2\partial\eta^2}+s_b^4\frac{\partial^4\bar{w}}{\partial\eta^4}=\\&s_b^2\left(\frac{\partial^2\bar{\varphi}}{\partial\eta^2}\cdot\frac{\partial^2\bar{w}}{\partial\xi^2}-2\frac{\partial^2\bar{\varphi}}{\partial\xi\partial\eta}\cdot\frac{\partial^2\bar{w}}{\partial\xi\partial\eta}+\frac{\partial^2\bar{\varphi}}{\partial\xi^2}\cdot\frac{\partial^2\bar{w}}{\partial\eta^2}\right)\\&+R_x\frac{\partial^2\bar{w}}{\partial\xi^2}+R_y s_b^2\frac{\partial^2\bar{w}}{\partial\eta^2}-\frac{\partial^2\bar{w}}{\partial\tau^2}+\bar{p}_a\\&+\bar{F}_{\mathrm{AABH}}\delta[(\xi-\xi_A)(\eta-\eta_A)]\end{aligned}\tag{4}$$

$$\begin{aligned}&\frac{\partial^4\bar{\varphi}}{\partial\xi^4}+2s_b^2\frac{\partial^4\bar{\varphi}}{\partial\xi^2\partial\eta^2}+s_b^4\frac{\partial^4\bar{\varphi}}{\partial\eta^4}=\\&12(1-\nu^2)\left[\left(\frac{\partial^2\bar{w}}{\partial\xi\partial\eta}\right)^2-\frac{\partial^2\bar{w}}{\partial\xi^2}\cdot\frac{\partial^2\bar{w}}{\partial\eta^2}\right]\end{aligned}\tag{5}$$

where $\bar{p}_a=-\left(\lambda\frac{\partial\bar{w}}{\partial\xi}+\sqrt{\lambda R_M}\frac{\partial\bar{w}}{\partial\tau}\right)$.

Eqs. (4) and (5) were solved using the Galerkin's method developed by Dowell.[31] For a simply supported panel, the following displacement is assumed[31,32]:

$$\bar{w}(\xi,\eta,\tau)=\sum_{m=1}^{M}q_m(\tau)\sin(m\pi\xi)\sin(\pi\eta)\tag{6}$$

The airy stress $\bar{\varphi}$ is determined by homogeneous solution $\bar{\varphi}_h$ and a specific solution $\bar{\varphi}_p$, that is, $\bar{\varphi}=\bar{\varphi}_h+\bar{\varphi}_p$. Based on Eq. (6) and combined with boundary conditions, the homogeneous solution and specific solution for Airy stress $\bar{\varphi}$ can be obtained, the specific solution process of $\bar{\varphi}$ can refer to literature.[31] Then, following the Galerkin's method we multiply the Eq. (4) by the basic function $\sin(n\pi\xi)\sin(\pi\eta)$, $(n=1,2,\cdots,M)$ and integrate along the chord and spanwise directions of the panel for ξ and η in the interval $[0,1]$. The result of ordinary differential equation is directly given as follows:

$$\begin{aligned}&\frac{\mathrm{d}^2 q_n}{\mathrm{d}\tau^2}=-\lambda\left\{\sum_{m=1,m\neq n}^{M}\frac{2nm}{n^2-m^2}\left[1-(-1)^{n+m}\right]q_m\cdot+\right.\\&\left.\sqrt{\frac{\mu}{Ma\lambda}}\cdot\frac{\mathrm{d}q_n}{\mathrm{d}\tau}\right\}-3\pi^4(1-\nu^2)\left\{\frac{q_n}{2}\left[n^2A+s_b^2B\right]\right.\\&\left.+s_b^4\left(C_n+D_n+\frac{E_n}{4}-\frac{F_n}{2}\right)\right\}-\bar{F}^*_{\mathrm{AABH},n}\\&-q_n\pi^4\left(n^2+s_b^2\right)^2-R_x\pi^2n^2q_n-R_y\pi^2s_b^2q_n\\&(n=1,2,\cdots,M)\end{aligned}\tag{7}$$

Eq. (7) is a set of coupled ordinary differential equations in time. They are solved by a direct numerical integration. The expressions of $A-F_n$ and $\bar{F}^*_{\mathrm{AABH},n}$ are given in Appendix B.

2.2. Dynamic equations of AABH

For the forces F_{AABH} exerted on the panel by the AABH, an equivalent calculation method is introduced. After discretization using FEM, the dynamic equation of AABH structure can be expressed as:

$$\boldsymbol{M}_A\ddot{\boldsymbol{w}}_A+\boldsymbol{C}_A\dot{\boldsymbol{w}}_A+\boldsymbol{K}_A\boldsymbol{w}_A=\boldsymbol{0}\tag{8}$$

where $\boldsymbol{M}_A$, $\boldsymbol{C}_A$, $\boldsymbol{K}_A$ are mass, damping and stiffness matrices of AABH, respectively. $\boldsymbol{w}_A$ is a $N_A\times 1$ vector of the nodal displacement corresponding to the AABH structure.

Through modal analysis of Eq. (8) after ignoring the damping term, the modal vectors of the AABH can be obtained.

Modal analysis can be carried out based on two different kinds of boundary conditions: one with free boundary condition and the other with the interface with host structure fixed. In this study, the later was used in modal analysis of the AABH.

Due to the relatively small interfacial area between the panel and AABH in comparison to the bending wavelength, it is assumed that the motion on the interface is predominantly governed by the displacement $w(x_A, y_A)$ of the panel at the center of the interface, (x_A, y_A). For simplicity, the motion is considered solely along the z-axis. When the AABH is installed on the panel, the displacement of the AABH, $\boldsymbol{w}_A$, is the sum of the elastic displacement of the AABH and the translational displacement induced by $w(x_A, y_A)$ at the installation point, and thus can be expressed as follows[25]:

$$\boldsymbol{w}_A = \boldsymbol{\phi}_A \boldsymbol{q}_A + \{1\} w(x_A, y_A) \tag{9}$$

where $\boldsymbol{\phi}_A$ is the modal matrix of the AABH normalized with respect to the mass matrix, $\boldsymbol{q}_A$ is a $L \times 1$ vector of the modal coordinate of AABH, and $\{1\}$ is the vector of $N_A \times 1$ with all the components equal to 1. Obviously, the first term is the elastic displacement and the second term is translational rigid displacement.

By substituting Eq. (9) into the dynamic equation of AABH and simplifying it, we can obtain:

$$\boldsymbol{I}\ddot{\boldsymbol{q}}_A + [2\omega_A \zeta_A]\dot{\boldsymbol{q}}_A + [\omega_A^2]\boldsymbol{q}_A = \boldsymbol{F} \tag{10}$$

where $\boldsymbol{I}$ is a $L \times L$ unit matrix. $[2\omega_A\zeta_A]$ is a $L \times L$ diagonal matrix with each diagonal element denoted as $2\omega_{Ai}\zeta_{Ai}$, where ω_{Ai} and ζ_{Ai} are respectively the ith frequency and modal damping ratio of AABH. $[\omega_A^2]$ is also a $L \times L$ diagonal matrix, and each diagonal element is ω_{Ai}^2. The modal force $\boldsymbol{F}$ can be expressed as:

$$\boldsymbol{F} = -\boldsymbol{\phi}_A^{\mathrm{T}} \boldsymbol{M}_A \{1\} \ddot{w}(x_A, y_A) \tag{11}$$

The F_{AABH} is the reactive force from the AABH and can be expressed as:

$$\begin{aligned} F_{\mathrm{AABH}} &= -\{1\}^{\mathrm{T}} \boldsymbol{M}_A \ddot{\boldsymbol{w}}_A = \\ &-\{1\}^{\mathrm{T}} \boldsymbol{M}_A \boldsymbol{\phi}_A \ddot{\boldsymbol{q}}_A - \{1\}^{\mathrm{T}} \boldsymbol{M}_A \{1\} \ddot{w}(x_A, y_A) \end{aligned} \tag{12}$$

In Eq. (11) and Eq. (12), $\boldsymbol{\phi}_A^{\mathrm{T}} \boldsymbol{M}_A \{1\}$ is the modal participation factor of different modes in the interaction between AABH and the panel due to the translational motion w, which will be discussed subsequently. Additionally, $\{1\}^{\mathrm{T}} \boldsymbol{M}_A \{1\}$ is the total mass of AABH, denoted as m_A, that is, $\{1\}^{\mathrm{T}} \boldsymbol{M}_A \{1\} = m_A$. Obviously, the first term on the right-hand side of Eq. (12) is the sum of the inertial forces of the elastic modes, while the second term is the inertial force of the translational rigid mode of the AABH.

2.3. Solution of coupled system

Eqs. (7) and (10) are the governing equations of the coupled system with finite degrees of freedom after discretization. The two sets of ordinary differential equations are solved alternatively in the time domain. The temporal functions $q_n(\tau)$ and $\ddot{q}_n(\tau)$ are obtained by solving Eq. (7) using the four-order Runge-Kutta method (RK4). Substitution of $q_n(\tau)$ and $\ddot{q}_n(\tau)$ into the Eq. (6) gives the displacement $w(x, y)$ and acceleration $\ddot{w}(x, y)$ of the panel, and the acceleration $\ddot{w}(x_A, y_A)$ at the installation position of the AABH. Substituting $\ddot{w}(x_A, y_A)$ into Eq. (11) provides the modal force $\boldsymbol{F}$, and solution of Eq. (10) gives the modal coordinates $\boldsymbol{q}_A$ and modal acceleration $\ddot{\boldsymbol{q}}_A$ of AABH. By substituting $\ddot{\boldsymbol{q}}_A$ and $\ddot{w}(x_A, y_A)$ into Eq. (12), the force F_{AABH} can be obtained for the next time step in solution of Eq. (7). This iterative process is repeated until convergence criteria are satisfied. A flowchart of the iteration process is illustrated in Fig. 2.

The investigation of energy transfer between the panel and AABH necessitates the assessment of quantities like mechanical energy dissipation and input. For the AABH structure, the transient kinetic energy $\mathrm{Ek}_{\mathrm{AABH}}$ and potential energy $\mathrm{EP}_{\mathrm{AABH}}$ can be expressed as:

$$\begin{cases} \mathrm{Ek}_{\mathrm{AABH}} = \frac{1}{2} \dot{\boldsymbol{q}}_A^{\mathrm{T}} \boldsymbol{\phi}_A^{\mathrm{T}} \boldsymbol{M}_A \boldsymbol{\phi}_A \dot{\boldsymbol{q}}_A = \frac{1}{2} \sum_{i=1}^{L} \dot{q}_i^2 \\ \mathrm{EP}_{\mathrm{AABH}} = \frac{1}{2} \boldsymbol{q}_A^{\mathrm{T}} \boldsymbol{\phi}_A^{\mathrm{T}} \boldsymbol{K}_A \boldsymbol{\phi}_A \boldsymbol{q}_A = \frac{1}{2} \sum_{i=1}^{L} \omega_i^2 q_i^2 \end{cases} \tag{13}$$

The energy consumed by the AABH structure can be expressed as:

$$\mathrm{ED}_{\mathrm{AABH}} = \int_0^t \dot{\boldsymbol{q}}_A^{\mathrm{T}} \boldsymbol{\phi}_A^{\mathrm{T}} \boldsymbol{C}_A \boldsymbol{\phi}_A \dot{\boldsymbol{q}}_A \mathrm{d}t = \sum_{i=1}^{L} 2\omega_{Ai}\zeta_{Ai} \int_0^t \dot{q}_i^2 \mathrm{d}t \tag{14}$$

The energy input provided by the airflow before time t can be expressed as:

$$\mathrm{EI}_{\mathrm{airflow}} = \int_0^t \int_0^b \int_0^a p_a \dot{w}(x, y, t) \mathrm{d}x \mathrm{d}y \mathrm{d}t \tag{15}$$

2.4. Verification of accuracy of aeroelastic analysis

To validate the accuracy of the model calculations, the aeroelastic response results for a simply supported square panel were obtained and compared to other results in the Ref. 32. The geometry, material, and inflow properties of the investigated 3-D simply supported panel are set as follows: $a/b = 0.5$, $h/a = 1/300$, $\rho = 2\,750\,\mathrm{kg/m^3}$, $E = 7.1 \times 10^{10}\,\mathrm{Pa}$,

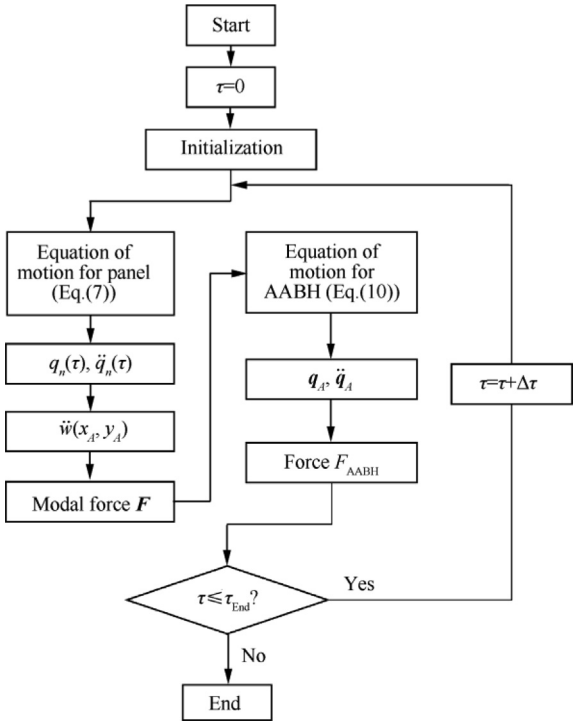

Fig. 2 Flowchart of iteration process.

$\upsilon = 0.3$, and $\mu/Ma = 0.01$. The results of the bifurcation diagram for the aeroelastic response at the monitoring point $(0.75a, 0.5b)$ on the panel are presented in Fig. 3, showcasing excellent agreement between the results of the present study and those given in the Ref. 32.

3. Simulation model and its approximation

3.1. Panel model and convergence verification

For the panel, the length, width, and thickness are $a = 500\,\text{mm}$, $b = 500\,\text{mm}$, and $h = 1.33\,\text{mm}$ respectively. The material parameters are listed in Table 1. In this study, the flow condition is characterized by specific assumptions regarding the ratio $\mu/Ma = 0.1$, the in-plane external force $R_x = R_y = -\pi^2$, and a varying λ. To accurately determine the aeroelastic response, an initial investigation into the convergence of the panel response across varying the M, is conducted. The calculated bifurcation diagram of aerodynamic response of the pure panel at the monitoring point $(0.65a, 0.5b)$ with different M is presented in Fig. 4. It's important to highlight that a very fine interval of λ has been employed near the critical flutter boundary within the bifurcation diagram, aiming to minimize computational errors significantly.

The results indicate that satisfactory computational accuracy can be obtained when $M = 6$, which is also consistent with the conclusion in Ref. 31. Consequently, this selection will be utilized in the subsequent analysis of the aeroelastic response of the panel incorporating the AABH. The critical flutter boundary of the panel is approximately $\lambda = 439$, as shown in Fig. 4. Furthermore, the flutter oscillation spectrum of the panel, observed at a slightly greater value than the critical flutter boundary, $\lambda = 441$, is showcased in Fig. 5, with the frequency determined to be around 52.2 Hz.

3.2. AABH model and convergence verification

The designed AABH structure is illustrated in Fig. 6. It features an asymmetric rectangular configuration with ABH characteristics. A damping layer, with a constant thickness h_d and width of d, is bonded along its edge. The AABH structure is segmented into three main parts: a central uniform rectangular platform with a constant thickness h_0, four regions with varying thickness, and another platform of constant thickness h_1. The change function in the variable thickness region is described as follows:

$$h(x) = \varepsilon_j x^r + h_0,\ j = 1, 2, 3, 4 \tag{16}$$

where $\varepsilon_j = \frac{h_0 - h_1}{(d_j)^r}$.

The geometric parameters of the AABH implemented in this study are outlined in Table 2, while the material parameters of the AABH are detailed in Table 1. Numerical analysis of the AABH is carried out using the commercial software, ABAQUS. The mesh size is carefully selected to ensure there are more than ten elements per wavelength, enabling an accurate description of vibration details near the AABH tip. The mesh is divided in a non-uniform manner to adapt to the geometric changes in the ABH region, and the damping layer is guaranteed to share common nodes at the interface. The finite element model is shown in Fig. 7, which adopts C3D20R 3-D elements with 20 nodal points. The mesh of the AABH FEM model comprises 24 472 nodes and 4 410 elements.

The mass of the panel is 0.901 kg. In contrast, the total mass of the AABH structure, including the damping layer, amounts to 0.054 kg, which represents 6.0% of the panel's mass. To mitigate the impact of the additional mass introduced by the AABH structure on the analysis, an idealized equivalent mass model, mirroring the AABH structure's weight (0.054 kg), is employed. This model is strategically positioned at the same location as the AABH for comparative analysis.

The accuracy of the AABH model significantly influences the computational precision of the combined system, which includes both the panel and the AABH. Specifically, the accuracy of the AABH model is determined by the order L, the number of modes used is Eq. (10). In order to confirm the convergence, the bifurcation diagram depicting the aeroelastic response of the combined system is computed with $L = 5$, $L = 9$, $L = 13$ and $L = 16$, respectively, and the results are shown in Fig. 8. These results demonstrate that satisfactory precision is attained when $L = 13$, as the discrepancy between the curve for $L = 13$ and that for $L = 16$ is minimal. Nonetheless, for the enhanced design and application of AABH in augmenting aeroelastic stability, a deeper exploration into how each individual mode affects the aeroelastic response of the combined system is deemed valuable and warrants further investigation.

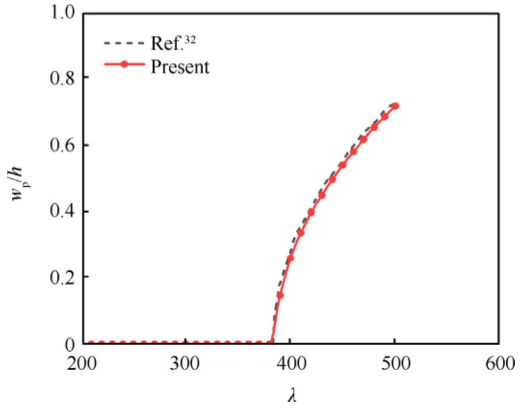

Fig. 3 Comparison of bifurcation diagrams for aeroelastic response of pure panel.

3.3. Factors that influence AABH model convergence

The influence of the AABH on the panel is mediated through the force F_{AABH} in Eq. (12), which consists of two parts: the first being reactive force by the elastic modes and the second being the reactive force due to the rigid motion of AABH. Therefore, to elucidate how each individual mode impacts the aeroelastic response of the combined system, it is crucial to analyze the force generated by each AABH mode. As defined in Ref. 33, the modal participation factor γ_i of the ith mode is defined as follows:

$$\boldsymbol{\phi}_A^{\mathrm{T}} \boldsymbol{M}_A \{1\} = [\phi_{Ai}]^{\mathrm{T}} \boldsymbol{M}_A \{1\} = \{\gamma_i\} \tag{17}$$

Table 1 Structural material parameters.

Structure	Young's modulus (Pa)	Density (kg/m^3)	Poisson's ratio	Material loss factor
Panel	7.1×10^{10}	2 710	0.346	0.001
AABH	9×10^9	2 700	0.346	0.001
Damping	2×10^8	1 800	0.45	0.3

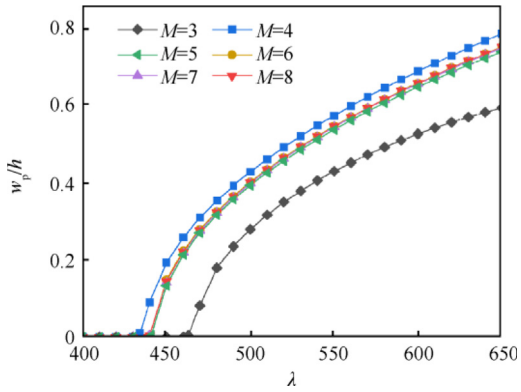

Fig. 4 Convergence calculation using different M.

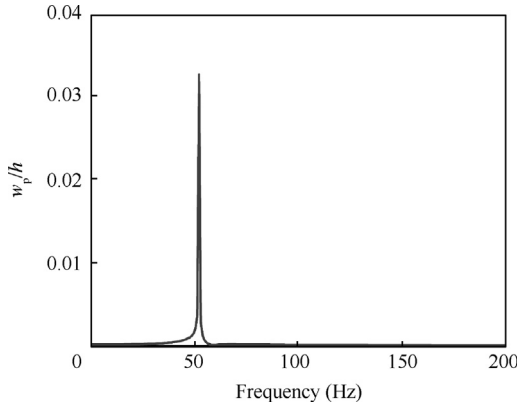

Fig. 5 Flutter frequency of the pure panel at $\lambda = 441$.

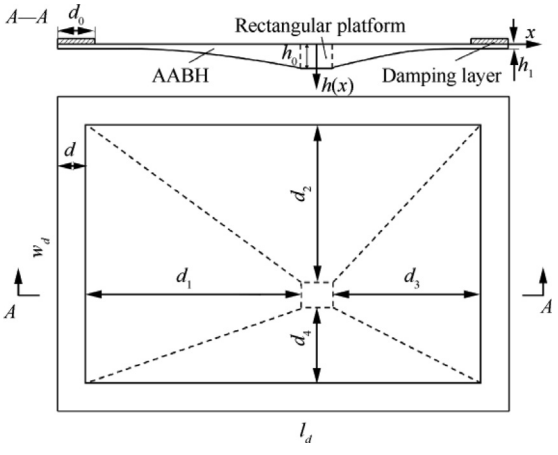

Fig. 6 Schematic of AABH structure.

Table 2 Geometric parameter table of AABH structure.

Parameter	Value
r	2.5
d(mm)	15
d_0(mm)	15
d_1(mm)	92
d_2(mm)	70
d_3(mm)	57
d_4(mm)	34
h_0(mm)	3
h_1(mm)	0.3
h_d(mm)	1
l_d(mm)	185
w_d(mm)	140

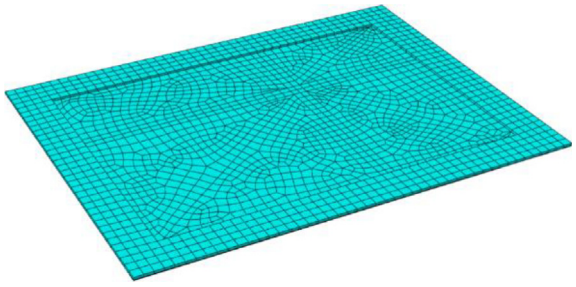

Fig. 7 Mesh of AABH.

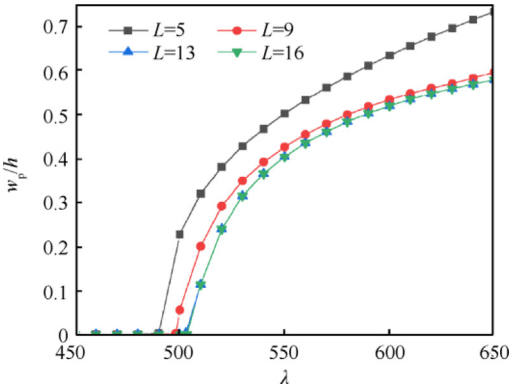

Fig. 8 Convergence calculation using different AABH mode numbers.

The modal effective mass of the ith mode of the AABH is defined as follows:

$$m_{Ai} = \frac{\left(\boldsymbol{\phi}_{Ai}^{\mathrm{T}} \boldsymbol{M}_A \{1\}\right)^2}{\boldsymbol{\phi}_{Ai}^{\mathrm{T}} \boldsymbol{M}_A \boldsymbol{\phi}_{Ai}} = \gamma_i^2 \tag{18}$$

In the equation mentioned, it is assumed that the modal vectors $\boldsymbol{\phi}_{Ai}$ have been normalized with respect to the mass matrix $\boldsymbol{M}_A$. Consequently, the total modal effective mass of the AABH can be expressed as the summation of all the modal effective masses, which is given by

$$\begin{aligned} \sum_{i=1}^{N_A} m_{Ai} &= \{1\}^{\mathrm{T}} \boldsymbol{M}_A \boldsymbol{\phi}_A \boldsymbol{\phi}_A^{\mathrm{T}} \boldsymbol{M}_A \{1\} \\ &= \{1\}^{\mathrm{T}} \boldsymbol{M}_A^{1/2} \left(\boldsymbol{M}_A^{1/2} \boldsymbol{\phi}_A\right) \left(\boldsymbol{M}_A^{1/2} \boldsymbol{\phi}_A\right)^{\mathrm{T}} \boldsymbol{M}_A^{1/2} \{1\} \\ &= \{1\}^{\mathrm{T}} \boldsymbol{M}_A \{1\} = m_A \end{aligned} \tag{19}$$

If only the first L modes are taken into consideration, the accumulative effective mass is smaller than the total mass of the AABH, m_A.

Assuming that a flutter oscillation occurs at a frequency of ω, the combination of Eqs. (10)–(12) yields the expression for the amplitude of the reactive force generated by the ith mode of the AABH in the frequency domain as follows:

$$\left|F_{\mathrm{AABH}(i)}\right| = \left|\{1\}^{\mathrm{T}} \boldsymbol{M}_A \boldsymbol{\phi}_{Ai} \ddot{q}_{Ai}\right| = \frac{m_{Ai}\omega^2}{\sqrt{\left(\omega_{Ai}^2 - \omega^2\right)^2 + \left(2\zeta_{Ai}\omega_{Ai}\omega\right)^2}} \left|\ddot{w}(x_A, y_A)\right| \tag{20}$$

Obviously, the force exerted by the ith mode of the AABH is contingent upon several factors: the modal mass m_{Ai}, the difference discrepancy between ω and ω_{Ai}, and the damping ratio ζ_{Ai}. The modal participation factors, modal effective mass, modal damping ratio and natural frequency of the AABH's 13 modes have been calculated and are listed in Table 3.

The results presented in Table 3 reveal that the 4th, 8th, and 10th modes possess relatively low modal masses, like the 7th and 11th modes. To assess the impact of these modes on computational accuracy, bifurcation diagrams for models incorporating all 13 modes, as well as those excluding some of these specific modes, are calculated and illustrated in Fig. 9 and Fig. 10. The diagrams clearly demonstrate that omitting the 4th, 8th, and 10th modes results in minimal computational error. While the 7th and 11th modes share comparable modal masses, the 7th mode exerts a more pronounced effect on accuracy, as illustrated in Fig. 10. This is attributed to its natural frequency being closer to the flutter oscillation frequency, which fluctuates between 52.2 Hz and 63.6 Hz as the parameter λ varies from 400 to 650. Furthermore, Fig. 9 indicates that the 8th mode slightly more significantly impacts accuracy than the

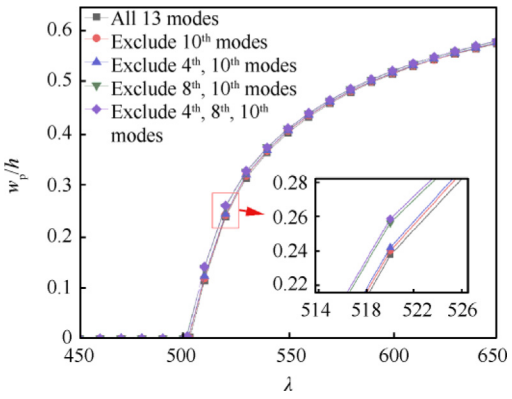

Fig. 9 Influence of different AABH modes on calculation (4th,8th,10th modes).

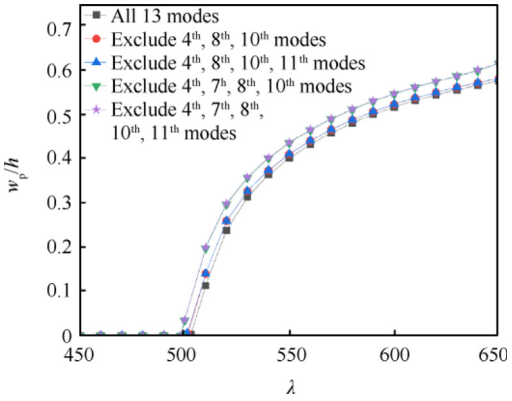

Fig. 10 Influence of different AABH modes on calculation (4th, 7th,8th,10th,11th modes).

Table 3 Parameters of first 13 modes (AABH).

Modal order	Modal participation factors	Modal effective mass	Frequency (Hz)	Modal damping ratio
1	0.092 0	0.008 47	21.73	0.025 75
2	0.030 8	0.000 95	27.68	0.030 51
3	0.091 2	0.008 31	31.01	0.030 52
4	0.005 5	0.000 03	43.42	0.031 80
5	0.077 8	0.006 05	46.68	0.041 55
6	0.020 7	0.000 43	57.55	0.057 78
7	0.014 5	0.000 21	69.84	0.051 55
8	−0.007 1	0.000 05	89.07	0.069 83
9	0.075 5	0.005 70	92.82	0.047 79
10	0.008 4	0.000 07	111.80	0.056 05
11	−0.013 8	0.000 19	125.10	0.075 57
12	−0.039 0	0.001 52	139.90	0.062 92
13	−0.024 9	0.000 62	145.10	0.062 02

4th and 10th modes, due to a combined effect of modal mass, frequency disparity, and damping ratio.

The total modal effective mass sums up to 32.6 g, constituting approximately 60% of the AABH's total mass. The remaining 40% of the AABH mass is attributed to higher order modes, which do not significantly contribute to flutter suppression. The modal damping ratio is a critical and pivotal parameter. An increase in the modal damping ratio can, on one hand, decrease the acting forces $|F_{\mathrm{AABH}(i)}|$ and, on the other hand, result in an increase in the consumed energy. The impact of the modal damping ratio warrants further discussion and analysis as future work, with the aim of optimizing the damping ratio parameters to enhance the suppression effect on aeroelastic responses.

4. Performance of AABH in panel flutter suppression

4.1. Aeroelastic responses and energy flow in combined system

Based on the parameters in Tables 1 and 2, the natural frequencies and modal damping ratios of the panel, the AABH and the combined system are also computed by commercial software, ABAQUS, and the results are plotted in Fig. 11, spanning a frequency range up to four times that of the critical flutter boundary. It is apparent that the modal damping ratios for nearly all modes have experienced a significant increase except for the mode at approximately 145 Hz.

The bifurcation diagrams for the pure panel, the combined structure of the panel and AABH, and the panel with an equivalent mass, have been computed, and their responses at the same monitoring point are illustrated Fig. 12. It is evident that attaching a mass can enhance the critical flutter boundary from $\lambda = 439$ to $\lambda = 455$ (yielding an improvement of about 3.6%), but the AABH demonstrates superior performance in suppressing panel flutter, extending the flutter boundary from $\lambda = 439$ to $\lambda = 504$ (an improvement of approximately 14.6%). Moreover, the oscillation amplitude of the combined structure is also reduced compared to that of the panel with an equivalent mass, which in turn is lower than that of the pure panel.

The parameter range depicted in Fig. 12 can be segmented into three distinct regions: Region A ($\lambda < 439$) where both the pure panel and the combined structure exhibit stability, Region B ($439 < \lambda \leqslant 504$) where the pure panel becomes unstable while the combined structure remains stable, and

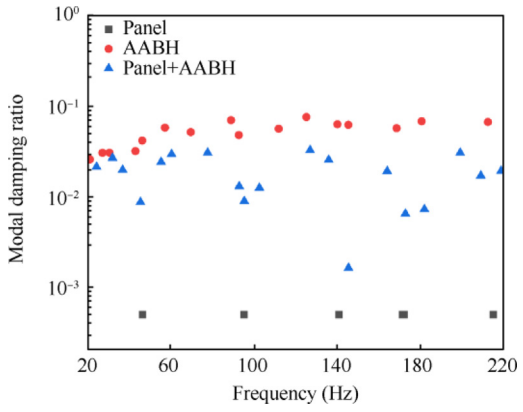

Fig. 11 Modal damping ratio of different structures.

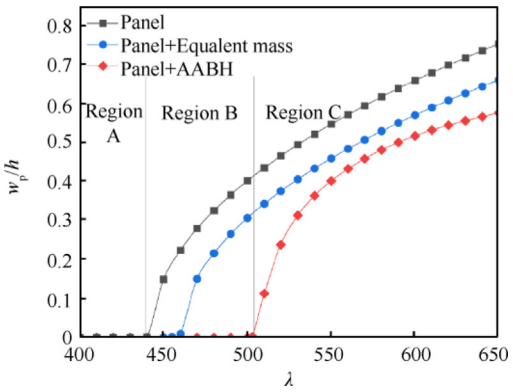

Fig. 12 Bifurcation diagrams for aeroelastic response of different panel configurations.

Region C ($\lambda > 504$) where both structures enter instability. The aeroelastic responses of both the pure panel and the combined structure within these three regions, corresponding to $\lambda = 420$, $\lambda = 475$ and $\lambda = 600$, respectively, are calculated and shown in Fig. 13. In conditions of stability, the structure returns to an equilibrium position from its initial state. Conversely, in a state of instability, it evolves into a Limit Cycle Oscillation (LCO).

To elucidate the mechanism behind the AABH's enhanced performance in panel flutter suppression, an examination of the energy dynamics within the combined structure was undertaken. At $\lambda = 600$, the energy influx from airflow, the energy dissipation by the AABH, and the transient total energies

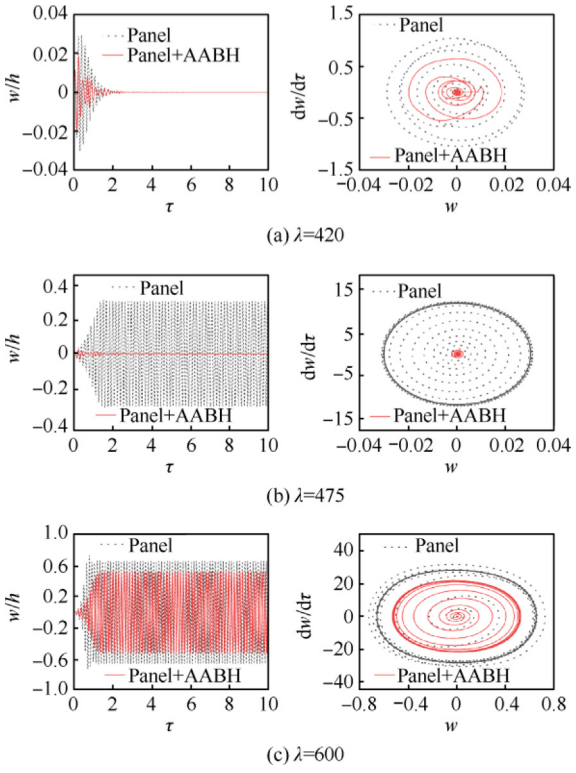

Fig. 13 Time history response results and phase plane of panel with and without AABH under different dynamic pressures.

within both the panel and the AABH, as formulated in Eqs. (13)–(15), are calculate and displayed in Fig. 14. It is observed that while both the energy input and consumption escalate over time, their differential largely remains constant. This constancy represents the cumulative energy stored within the panel and AABH in both kinetic and potential forms during the limit cycle oscillation.

4.2. Performance of AABH in comparison with TMD and NES

Given that both TMD and NES have been employed for panel flutter suppression, as referenced in Refs. 18,19,34 conducting a comprehensive comparison between the efficacy of AABH and these traditional methods is both meaningful and necessary. The performance characteristics of TMD and NES are primarily dictated by their mass, spring stiffness, and damping coefficient, detailed in Appendix C. For the TMD, optimal parameters based on the mass of the AABH and the vibration frequency of the panel at the flutter boundary are identified as $\bar{m}_{\mathrm{TMD}} = 0.06$, $\bar{k}_{\mathrm{TMD}} = 60$, and $\bar{c}_{\mathrm{TMD}} = 0.2$, respectively. Similarly, the NES parameters, as informed by Ref. 18, with optimal settings are defined as $\bar{m}_{\mathrm{NES}} = 0.06$, $\bar{k}_{\mathrm{NES}} = 90\,000$, and $\bar{c}_{\mathrm{NES}} = 0.2$, respectively. All damping subsystems considered for comparison constitute 6% of the panel weight and are mounted at identical positions. The bifurcation diagrams depicting the aeroelastic response at the same monitoring point $(0.65a, 0.5b)$ of pure panel, panel with equivalent mass, panel with TMD, panel with NES, and panel with AABH are calculated and illustrated in Fig. 15.

Remarkably, the panel integrated with NES exhibits two distinct critical flutter boundaries: one indicative of small amplitude limit cycle oscillation (LCO) and another for large amplitude LCO, with the initial flutter boundary aligning closely with that of the pure panel. This finding corroborates results from Ref. 18. Defining the second flutter boundary as characteristic of the panel with NES, the hierarchy from most to least stable structure is as follows: panel with NES, panel with AABH, panel with TMD, panel with equivalent mass, and finally, the pure panel.

Despite the NES displaying a higher second flutter boundary compared to the AABH, the amplitude of LCO of the panel with NES significantly exceeds that of the panel with AABH. When comparing the LCO amplitudes of different structures at a specified $\lambda = 550$, the ranking from smallest to largest amplitude is as follows: panel with AABH, panel with equivalent mass, panel with TMD, panel with NES, and finally, the pure panel. These findings underscore that the AABH outperforms other methodologies in terms of panel flutter suppression, offering a more effective solution for reducing LCO amplitudes and enhancing structural stability.

4.3. Improvement of AABH performance in panel flutter suppression

Geometrical modifications have been applied to the original AABH design to enhance its effectiveness in panel flutter suppression. The modified version, referred to as AABH-2, features updated parameters transitioning from $d_1 = 92\,\mathrm{mm}$, $d_2 = 70\,\mathrm{mm}$, $d_3 = 57\,\mathrm{mm}$, and $d_4 = 34\,\mathrm{mm}$, to $d_1 = 82\,\mathrm{mm}$, $d_2 = 60\,\mathrm{mm}$, $d_3 = 67\,\mathrm{mm}$, and $d_4 = 44\,\mathrm{mm}$, respectively. The modal damping ratio of Modal damping ratios of AABH and AABH-2 are depicted in Fig. 16, showing the variation of parameters will affect modal frequency and modal damping ratio, thereby affecting performance. Furthermore, the bifurcation diagram for the newly formed combined structure (panel with AABH-2) is also calculated and illustrated in Fig. 17. This diagram reveals that the new flutter boundary for the combined structure reaches $\lambda = 519$ (an 18.2% improvement over the pure panel), surpassing the performance of the original combined structure's $\lambda = 504$ (14.6% improve-

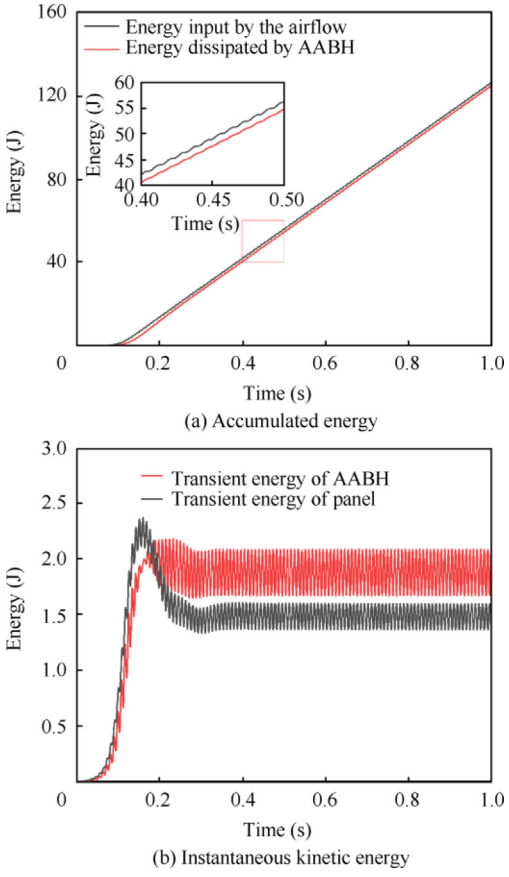

Fig. 14 Time history of energies at $\lambda = 600$.

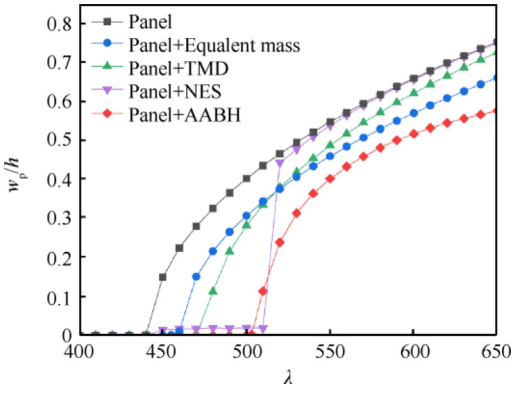

Fig. 15 Bifurcation diagrams for aeroelastic response of different panel configurations (comparison between AABH and traditional passive control structures).

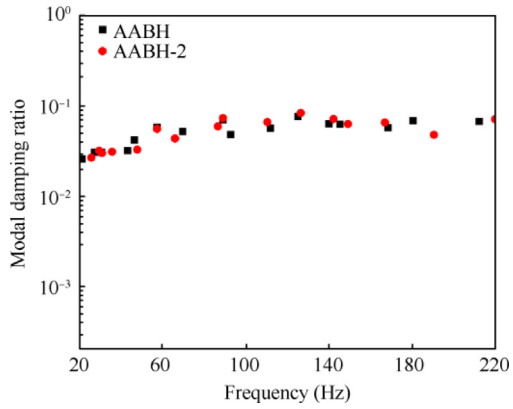

Fig. 16 Modal damping ratios of AABH and AABH-2.

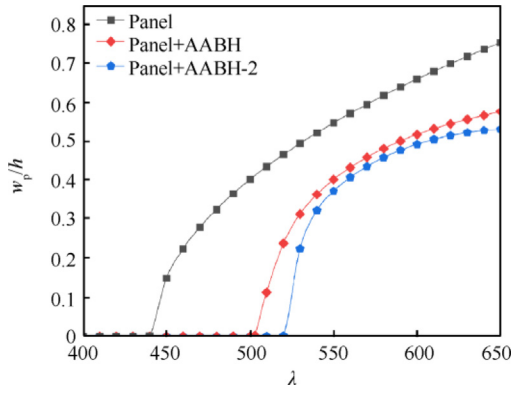

Fig. 17 Bifurcation diagrams for aeroelastic response of different panel configurations (Panel only, Panel with AABH, and Panel with AABH-2).

ment), thereby demonstrating the effectiveness of the geometrical modifications in further suppressing panel flutter.

The modal participation factors, modal effective mass, the modal damping ratio, and natural frequency of the 13 modes of the AABH-2 are calculated and detailed in Table 4. A notable observation from the data is the significant increase in modal effective masses for the low-order modes, which are proximal to the frequency of LCO, indicating enhanced responsiveness in this critical frequency range. The accumulative effective mass of the 13 modes of the AABH-2 is 32.3 g, which is virtually equivalent to that of the original AABH. However, the combined effective mass of the first 8 modes of AABH-2 reaches 30.6 g, showcasing a substantial enhancement over the 24.5 g cumulative effective mass of the initial 8 modes of the original AABH. This improvement underscores the principle that the flutter suppression capabilities of the AABH can be significantly advanced by augmenting the cumulative effective mass within the pertinent frequency spectrum.

The response amplitudes for different λ when AABH was placed at various positions on the panel are calculated. It can be observed from Fig. 18 that the effects corresponding to different λ and AABH installation positions are not consistent. However, both consistently show that a position shifted to the rear of the centerline, perpendicular to the direction of the airflow, is more favorable for flutter suppression of the panel. Based on the results, the installation position (ξ, η) of AABH is changed from (0.65, 0.50) to (0.60, 0.50) and the bifurcation diagram of the panel with AABH is calculated, as shown in Fig. 19. It shows that the change in installation position further improves the flutter suppression effectiveness of AABH. The impact of AABH at different installation positions on the critical boundary of panel flutter is also worth investigating in future work for further calculation and analysis.

Such findings not only highlight the potential for optimizing the AABH's flutter suppression performance but also provide valuable insights for guiding the future optimal design of AABH in mitigating panel flutter, emphasizing the strategic increase of effective mass in targeted frequency ranges and suitable installation position for heightened aeroelastic stability.

5. Conclusions

This research introduces a novel approach for the coupled aeroelastic analysis of panels subjected to supersonic airflow, enhanced with an add-on acoustic black hole to investigate

Table 4 Parameters of first 13 modes (AABH-2).

Modal order	Modal participation factors	Modal effective mass	Frequency (Hz)	Modal damping ratio
1	0.085 7	0.007 35	26.08	0.026 54
2	0.031 7	0.001 01	29.80	0.031 65
3	0.094 0	0.008 83	31.14	0.029 85
4	0.064 8	0.004 19	36.00	0.030 84
5	0.052 9	0.002 80	47.98	0.032 61
6	−0.011 8	0.000 14	57.44	0.055 15
7	0.005 8	0.000 03	65.97	0.043 26
8	0.079 1	0.006 25	86.42	0.058 80
9	−0.003 3	0.000 01	88.69	0.072 83
10	−0.010 0	0.000 10	109.71	0.065 61
11	−0.006 7	0.000 04	125.55	0.082 66
12	0.006 7	0.000 04	141.05	0.071 00
13	−0.039 2	0.001 54	147.83	0.062 45

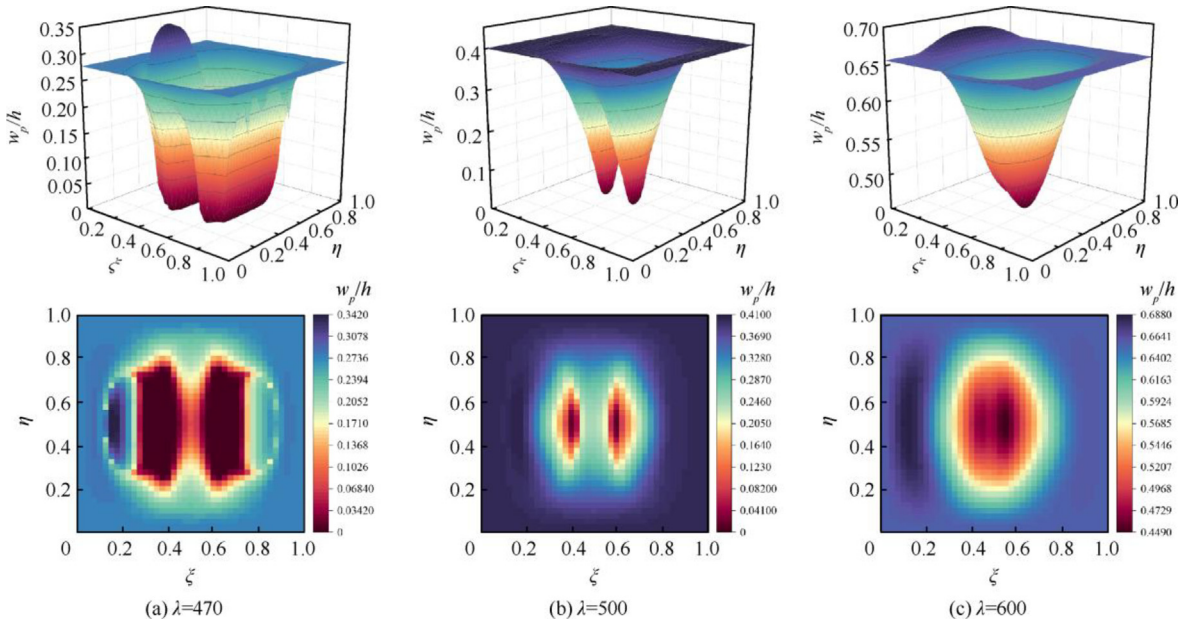

Fig. 18 Effects of installed position on the aeroelastic response for AABH.

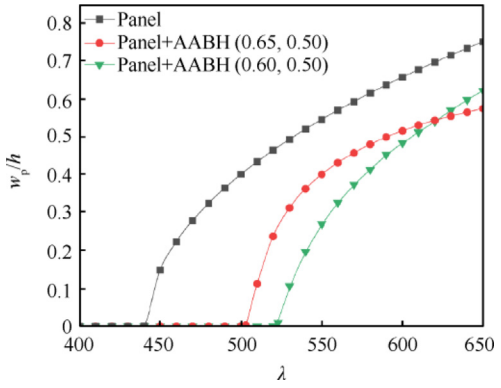

Fig. 19 Bifurcation diagrams for aeroelastic response of different panel configurations (Panel with AABH at different positions).

the system's aeroelastic response. Concluding remarks can be summarized as follows:

(1) The panel's aeroelastic equation was discretized utilizing the traditional Galerkin's method and subsequently solved through numerical integration. A numerical model of the AABH, derived via FEM, was simplified to a minimal number of degrees of freedom. The integration of the two substructures was achieved by coupling their interface displacements, and the combined system was analyzed through alternate numerical integration of the subsystems.

(2) An in-depth analysis of the interactive forces revealed that the modal effective mass, the frequency disparity between the panel's flutter oscillation and the AABH mode, and the AABH's modal damping ratio are critical in determining the impact of individual AABH modes on panel flutter suppression and the precision of numerical simulations.

(3) The findings demonstrate that the AABH significantly enhances the panel's critical flutter boundary by 14.6%, a marked improvement over the 3.6% enhancement provided by an equivalent mass. Moreover, the AABH outperforms both the tuned mass damper and nonlinear energy sink in terms of flutter suppression efficacy.

(4) By adjusting the AABH's geometrical parameters, its flutter suppression capabilities were further optimized, evidenced by an increase in the cumulative modal effective mass within the relevant frequency range. The installation position of AABH also determines its flutter suppression performance, the position behind the centerline perpendicular to the airflow direction is more conducive to the flutter suppression of the AABH. These insights provide valuable guidance for the optimal design of AABH, showcasing its potential in improving aeroelastic stability.

CRediT authorship contribution statement

Zhuogeng ZHANG: Writing – original draft, Software, Formal analysis, Data curation. **Hongli JI:** Supervision, Project administration, Funding acquisition, Conceptualization. **Jinhao QIU:** Writing – review & editing, Supervision, Methodology, Funding acquisition. **Kaihua YUAN:** Methodology, Data curation. **Li CHENG:** Writing – review & editing, Supervision.

Declaration of competing interest

The authors declare that they have no known competing financial interests or personal relationships that could have appeared to influence the work reported in this paper.

Acknowledgements

This study was co-supported by the National Key Research and Development Program of China (No. 2021YFB3400100), and the National Natural Science Foundation of China (Nos. 52235003 & U2241261).

Appendix A. Dimensionless parameters and variables

$$\bar{w}=\frac{w}{h},\xi=\frac{x}{a},\eta=\frac{y}{b},\tau=t\left(\frac{D}{\rho ha^4}\right)^{1/2},\bar{\varphi}=\frac{h}{D}\varphi,\beta=\sqrt{Ma^2-1},$$
$$R_M=\frac{\mu}{\beta},\lambda=\frac{2pa^3}{\beta D},\mu=\frac{\rho_a a}{\rho h},s_b=\frac{a}{b},\bar{F}_{\mathrm{AABH}}=\frac{a^3}{Dbh}F_{\mathrm{AABH}},$$
$$\bar{m}=\frac{m}{\rho hab},R_{x(y)}=\frac{p^{(a)}_{x(y)}a^2}{D}$$

Appendix B. Expressions of $A-F_n$ and $\bar{F}_{\mathrm{AABH},n}$

$$A=\sum_{m=1}^{M}\frac{\left(m^2+vs_b^2\right)}{1-v^2}q_m^2$$
$$B=\sum_{m=1}^{M}\frac{\left(vm^2+s_b^2\right)}{1-v^2}q_m^2$$

$$C_n=\sum_{m=1}^{M}\sum_{s=1}^{M}\sum_{r=1}^{M}q_mq_sq_rr^2\frac{m(s-m)}{\left[(s+m)^2+4s_b^2\right]^2}\left(\gamma_{(s+m)(r-n)}-\gamma_{(s+m)(r+n)}\right)$$
$$+\sum_{m=1}^{M}\sum_{s=1}^{M}\sum_{r=1}^{M}q_mq_sq_rr^2\frac{m(s+m)}{\left[(s-m)^2+4s_b^2\right]^2}\left(\gamma_{(s-m)(r-n)}-\gamma_{(s-m)(r+n)}\right)$$

$$D_n=\sum_{m=1}^{M}\sum_{s=1}^{M}\sum_{r=1}^{M}q_mq_sq_rr\frac{m(s-m)(s+m)}{\left[(s+m)^2+4s_b^2\right]^2}\left(\beta_{(s+m)(r+n)}+\beta_{(s+m)(n-r)}\right)$$
$$+\sum_{m=1}^{M}\sum_{s=1}^{M}\sum_{r=1}^{M}q_mq_sq_rr\frac{m(s+m)(s-m)}{\left[(s-m)^2+4s_b^2\right]^2}\left(\beta_{(s-m)(r+n)}+\beta_{(s-m)(n-r)}\right)$$

$$E_n=\sum_{m=1}^{M}\sum_{s=1}^{M}\sum_{r=1}^{M}q_mq_sq_r\frac{m(s-m)(s+m)^2}{\left[(s+m)^2+4s_b^2\right]^2}\left(\gamma_{(s+m)(r-n)}-\gamma_{(s+m)(r+n)}\right)$$
$$+\sum_{m=1}^{M}\sum_{s=1}^{M}\sum_{r=1}^{M}q_mq_sq_r\frac{m(s+m)(s-m)^2}{\left[(s-m)^2+4s_b^2\right]^2}\left(\gamma_{(s-m)(r-n)}-\gamma_{(s-m)(r+n)}\right)$$

$$F_n=\sum_{m=1}^{M}\sum_{s=1}^{M}\sum_{r=1}^{M}q_mq_sq_r\frac{m}{s+m}\left(\gamma_{(s+m)(r-n)}-\gamma_{(s+m)(r+n)}\right)$$
$$+\sum_{m=1}^{M}\sum_{s=1}^{M}\sum_{r=1}^{M}q_mq_sq_r\frac{m}{s-m}\left(\gamma_{(s-m)(r-n)}-\gamma_{(s-m)(r+n)}\right)$$

$$\bar{F}^{*}_{\mathrm{AABH},n}=4\bar{F}_{\mathrm{AABH}}\sin\left(n\pi\xi_A\right)\sin\left(\pi\eta_A\right)$$

where

$$\gamma_{(p)(q)}=\begin{cases}2,p=q=0\\1,p=q\neq0\\-1,p=-q\neq0\\0,p\neq q\&p\neq-q\end{cases},\beta_{(p)(q)}=\begin{cases}1,p=q\neq0\\-1,p=-q\neq0\\0,p=q=0\\0,p\neq q\&p\neq-q\end{cases}.$$

Appendix C. Definition of parameters of TMD and NES

$$\bar{m}_{\mathrm{TMD}}=\frac{m_{\mathrm{TMD}}}{\rho hab},\bar{c}_{\mathrm{TMD}}=c_{\mathrm{TMD}}\times\sqrt{\frac{a^2}{\rho hDb^2}},\bar{k}_{\mathrm{TMD}}=k_{\mathrm{TMD}}\times\frac{a^3}{Db}$$

where the m_{TMD}, c_{TMD}, and k_{TMD} are the mass, damping, and stiffness parameters of TMD structure, respectively.

$$\bar{m}_{\mathrm{NES}}=\frac{m_{\mathrm{NES}}}{\rho hab},\bar{c}_{\mathrm{NES}}=c_{\mathrm{NES}}\times\sqrt{\frac{a^2}{\rho hDb^2}},\bar{k}_{\mathrm{NES}}=k_{\mathrm{NES}}\times\frac{a^3h^2}{Db}$$

where the m_{NES}, c_{NES}, and k_{NES} are the mass, damping, and stiffness parameters of NES structure, respectively.

References

1. Sharma N, Mohapatra S, Kumar EK, et al. Geometrically nonlinear aeroelastic flutter characteristic of laminated composite shell panels under supersonic flow. *Int J Appl Mech* 2023;**15**(4):2350029.
2. Amirzadegan S, Mousavi Safavi SM, Jafarzade A. Supersonic panel flutter analysis assuming effects of initial structural stresses. *J Inst Eng Ind Ser C* 2019;**100**(5):833–9.
3. Scott R, Weisshaar T. Controlling panel flutter using adaptive materials. Reston: AIAA; 1991. Report No.: AIAA-1991-1067.
4. Ibrahim HH, Yoo HH, Lee KS. Aero-thermo-mechanical characteristics of imperfect shape memory alloy hybrid composite panels. *J Sound Vib* 2009;**325**(3):583–96.
5. Ibrahim HH, Yoo HH, Lee KS. Thermal buckling and flutter behavior of shape memory alloy hybrid composite shells. *J Aircr* 2009;**46**(3):895–902.
6. Tang W, Wu J, Shi ZK. Identification of reduced-order model for an aeroelastic system from flutter test data. *Chin J Aeronaut* 2017;**30**(1):337–47.
7. Cunha-Filho AG, Briend YPJ, de Lima AMG, et al. An efficient iterative model reduction method for aeroviscoelastic panel flutter analysis in the supersonic regime. *Mech Syst Signal Process* 2018;**104**:575–88.
8. Cunha-Filho AG, de Lima AMG, Donadon MV, et al. Flutter suppression of plates using passive constrained viscoelastic layers. *Mech Syst Signal Process* 2016;**79**:99–111.
9. Moon SH, Kim SJ. Active and passive suppressions of nonlinear panel flutter using finite element method. *AIAA J* 2001;**39**(11):2042–50.
10. Verstraelen E, Habib G, Kerschen G, et al. Experimental passive flutter suppression using a linear tuned vibration absorber. *AIAA J* 2016;**55**(5):1707–22.
11. Pacheco DRQ, Marques FD, Ferreira AJM. Panel flutter suppression with nonlinear energy sinks: numerical modeling and analysis. *Int J Non Linear Mech* 2018;**106**:108–14.
12. Lee YS, Vakakis AF, Bergman LA, et al. Suppression aeroelastic instability using broadband passive targeted energy transfers, part 1: theory. *AIAA J* 2007;**45**(3):693–711.
13. Lee YS, Kerschen G, McFarland DM, et al. Suppressing aeroelastic instability using broadband passive targeted energy transfers, part 2:experiments. *AIAA J* 2007;**45**(10):2391–400.
14. Gourdon E, Alexander NA, Taylor CA, et al. Nonlinear energy pumping under transient forcing with strongly nonlinear coupling: theoretical and experimental results. *J Sound Vib* 2007;**300**(3–5):522–51.
15. Vakakis AF. Inducing passive nonlinear energy sinks in vibrating systems. *J Vib Acoust* 2001;**123**(3):324–32.
16. Gendelman OV, Vakakis AF, Bergman LA, et al. Asymptotic analysis of passive nonlinear suppression of aeroelastic instabilities of a rigid wing in subsonic flow. *SIAM J Appl Math* 2010;**70**(5):1655–77.
17. Lu Z, Wang ZX, Lv XL. A review on nonlinear energy sink technology. *J Vib Shock* 2020;**39**(4):1–16 [Chinese].
18. Zhou J, Xu ML, Yang ZC, et al. Suppression of panel flutter response in supersonic airflow using a nonlinear vibration absorber. *Int J Non Linear Mech* 2021;**133**:103714.
19. Zhou J, Xu ML, Yang ZC, et al. Suppressing nonlinear aeroelastic response of laminated composite panels in supersonic airflows using a nonlinear energy sink. *Chin J Aeronaut* 2021;**34**(2):376–85.

20. Bowyer EP, Krylov VV. Experimental investigation of damping flexural vibrations in glass fibre composite plates containing one- and two-dimensional acoustic black holes. *Compos Struct* 2014;**107**:406–15.
21. McCormick CA, Shepherd MR. Design optimization and performance comparison of three styles of one-dimensional acoustic black hole vibration absorbers. *J Sound Vib* 2020;**470**:115164.
22. Huang W, Ji HL, Qiu JH, et al. Wave energy focalization in a plate with imperfect two-dimensional acoustic black hole indentation. *J Vib Acoust* 2016;**138**(6):061004.
23. Zhou T, Cheng L. A resonant beam damper tailored with Acoustic Black Hole features for broadband vibration reduction. *J Sound Vib* 2018;**430**:174–84.
24. Ji HL, Wang N, Zhang C, et al. A vibration absorber based on two-dimensional acoustic black holes. *J Sound Vib* 2021;**500**:116024.
25. Ji HL, Zhao XN, Wang N, et al. A circular eccentric vibration absorber with circumferentially graded acoustic black hole features. *J Vib Acoust* 2022;**144**(2):021014.
26. Park S, Lee JY, Jeon W. Vibration damping of plates using waveguide absorbers based on spiral acoustic black holes. *J Sound Vib* 2022;**521**:116685.
27. Zhang ZG, Ji HL, Tao CC, et al. Suppression of panel flutter in supersonic flow based on acoustic black hole as a linear energy sink. *J Sound Vib* 2024;**571**:118030.
28. Xie CC, An C, Liu Y, et al. Static aeroelastic analysis including geometric nonlinearities based on reduced order model. *Chin J Aeronaut* 2017;**30**(2):638–50.
29. Sun QZ, Xing YF, Liu B, et al. Accurate closed-form eigensolutions of three-dimensional panel flutter with arbitrary homogeneous boundary conditions. *Chin J Aeronaut* 2023;**36**(1):266–89.
30. Xie D, Xu M. Three-dimensional panel nonlinear flutter analysis based on proper orthogonal decomposition method. *Eng Mech* 2015;**32**(1):1–9 [Chinese].
31. Dowell EH. Nonlinear oscillations of a fluttering plate. *AIAA J* 1966;**4**(7):1267–75.
32. Xie D, Xu M, Dai HH, et al. Proper orthogonal decomposition method for analysis of nonlinear panel flutter with thermal effects in supersonic flow. *J Sound Vib* 2015;**337**:263–83.
33. Wijker J. *Spacecraft structures*. Berlin: Springer-Verlag; 2008.
34. Zhao H, Cao D. Suppression of supersonic flutter of laminted composite panel using dynamic absorber device and its optimal design. *Aerosp Sci Technol* 2015;**47**:75–85.